Original Article

A facile synthesis of SnS_2/g-C_3N_4 S-scheme heterojunction photocatalyst with enhanced photocatalytic performance

Thanh Huong Nguyen Thi, Ha Tran Huu, Hung Nguyen Phi, Van Phuc Nguyen, Quoc Dat Le, Lan Nguyen Thi, Thi Thuy Trang Phan, Vien Vo[*]

Faculty of Natural Sciences, Quy Nhon University, 170 An Duong Vuong, Quy Nhon, Binh Dinh, 55000, Viet Nam

ABSTRACT

Constructing appropriate heterojunction systems has been considered the most promising among different methods for achieving effective charge transfer and separation to improve photocatalytic performance. Herein, SnS_2/g-C_3N_4 composites consisting of SnS_2 nanosheets loaded on a porous g-C_3N_4 matrix were successfully prepared *via* direct calcination from the precursors of tin (IV) chloride and thiourea. Under visible light, all the composites outperformed pure SnS_2 and g-C_3N_4 in terms of Rhodamine B (RhB) photodegradation, and the highest removal efficiency after 6 h of irradiation was 92.22%. Their photocatalytic performance was significantly enhanced because of the positive synergistic relationship between semiconductors (SnS_2 and g-C_3N_4) and the rational Step-scheme charge transfer mechanism. Thus, these composites contributed to the strong redox power, high migration efficiency, and extended lifetime of photogenerated carriers.

1. Introduction

Among the emerging research topics, photocatalysis has been influential and popular due to its promising multi-adaptation in the energy and environment fields. Numerous visible light-induced photocatalysts, such as SnO_2, CdS, WO_3, MoS_2, WS_2, and graphitic carbon nitride (g-C_3N_4), have been investigated to promote photocatalytic activities. Among them, g-C_3N_4, a famous metal-free polymeric semiconductor catalyst, is the most preferred because of its beneficial properties, including high physical and chemical stability, moderate bandgap energy (2.7 eV), and distinct electronic structure [1]. However, g-C_3N_4 insufficiently utilizes light, has a limited surface area, and yields a quick photoexcited electron–hole recombination rate, so it is limited by its poor photocatalytic ability [2]. To address these weaknesses, researchers applied some critical scientific solutions, such as element doping into g-C_3N_4 [3] and preparing g-C_3N_4 composites with other semiconductors (metal sulfide [4], metallic oxide [5], and graphene category [6]).

Tin disulfide (SnS_2) is a transition metal dichalcogenide semiconductor with a conventional two-dimensional (2D) layered structure; it has been extensively investigated because of its low price, nontoxicity, and unique physicochemical characteristics [1,7]. It also has a narrow bandgap of 1.89–2.35 eV, which provides a relatively strong visible light absorption ability [8]. However, single SnS_2 is limited by the severe recombination of photoexcited carriers, thereby impeding its widespread application in photocatalytic processes. To overcome this problem, researchers developed many SnS_2 modification methods; for example, coupling SnS_2 and g-C_3N_4 for constructing heterojunction photocatalysts is an efficient strategy to promote charge separation based on the photosynergistic effect and unique structural superiority [7,9,10].

To our knowledge, SnS_2/g-C_3N_4 composites have been designed and constructed using several methods, including ultrasonic dispersion [9], *in situ* hydrothermal method [8], and wet precipitation [7]. However, these synthesis routes are relatively complex, costly, and time-consuming. As such, a green, cost-effective, and convenient strategy for creating novel SnS_2/g-C_3N_4 heterojunctions with excellent performance is highly desirable. In this study, a new synthesis of SnS_2/g-C_3N_4 composites was developed using a one-pot calcination process in air atmosphere from a reaction mixture of tin (IV) chloride and thiourea. During the synthesis, g-C_3N_4 acted as a buffer to exfoliate SnS_2, whereas SnS_2 speeds up the

---

* Corresponding author.
E-mail address: vovien@qnu.edu.vn (V. Vo).
Peer review under responsibility of Vietnam National University, Hanoi.

breakdown of g-C$_3$N$_4$ at high temperatures, resulting in an N-deficiency form with improved charge transport. The photocatalytic activities of the obtained materials were examined by the degradation of Rhodamine B (RhB) dye under visible-light irradiation. Although RhB is widely applied for many industrial applications such as textiles, paper, and food, it has high toxicity and chemical stability, making it difficult to completely decompose by the traditional biochemical and physical-chemical methods [11]. This work proposes a promising strategy of employing SnS$_2$/g-C$_3$N$_4$ photocatalysts to eliminate RhB organic pollutant from dye-containing wastewater.

2. Experimental

2.1. Photocatalyst synthesis

SnS$_2$/g-C$_3$N$_4$ composites were fabricated *via* a simple calcination method from a precursor mixture of tin (IV) chloride (SnCl$_4$·2H$_2$O, ≥99%, Merck, Germany), and thiourea (CH$_4$N$_2$S, 99.5%, Merck, Germany). In a typical process, a mixture containing different weight ratios of tin (IV) chloride to thiourea (1:25, 1:30, and 1:35) was heated to 500 °C for 4 h. The obtained samples were labeled SCNx, where $x = 25$, 30, and 35, corresponding to the weight ratios of tin (IV) chloride to thiourea of 1:25, 1:30, and 1:35.

Pure SnS$_2$ (labeled SNS) was synthesized through the post-calcination of SCN30 at 650 °C in Ar gas for 2 h. Pure g-C$_3$N$_4$ (denoted as CN) was fabricated by directly annealing thiourea at 500 °C for 4 h at an increasing rate of 10 °C min^{-1}.

2.2. Physicochemical characterization

The crystalline structure of the as-prepared photocatalysts was examined through powder X-ray diffraction (XRD) using a D8 Advance X-ray diffractometer (Bruker AXS company, Germany) with a Cu-Kα (1.5406 A) as the referring source operated at 30 kV and 10 mA. The XRD scans were recorded in the 2θ range of 10–80° with a scanning rate of 7° min^{-1} and a step size of 0.01° (0.5s/step). The morphological characteristics of the as-synthesized materials were investigated using a scanning electron microscope (SEM, Nova Nano SEM 450), and a high-resolution transmission electron microscope (HR-TEM) was performed on a JEOL JEM-2100 F (JEOL, Japan) operating at 200 kV. The materials were coated with gold to prevent charge build-up during SEM examinations. The Fourier transform infrared (FTIR) spectra of the samples in the 400–4000 cm^{-1} range with a resolution of 4 cm^{-1} were obtained on an IR Prestige-21 spectrophotometer (Shimadzu) using KBr pellets containing a 1% weight sample. Thermogravimetric analysis (TGA) was conducted using a SETRAM LABSYS TG system with airflow and heating rate of 10 °C min^{-1}. X-ray photoelectron spectroscopy (XPS) data were obtained with a K-Alpha + Thermo Scientific system. A Shimadzu UV-2600 spectrophotometer with a spherical diffuse reflectance accessory was used to determine the bandgap energy of catalysts using UV–vis diffuse reflectance spectroscopy (DRS). The photoluminescence (PL) spectra of the synthesized samples were obtained using an iHR-550 fluorescence spectrophotometer stimulated at 355 nm.

2.3. Photocatalytic activity evaluation

The photocatalytic performance of the obtained samples was assessed on the basis of RhB photodegradation in an aqueous solution under visible light exposure. A typical experiment was conducted with a catalyst dose of 20 mg dispersed in 80 mL of RhB solution with a concentration of 20 mg/L. The obtained dispersion was continually stirred for 1.5 h in the dark to achieve the adsorption−desorption equilibrium. The mixed solution was then illuminated with a 60 W−220 V lamp with a UV cutoff filter (200−400 nm). At predefined intervals, an aliquot of the reaction solution was obtained and promptly centrifuged at 5000 rpm for 10 min to remove the catalyst. The residual concentration of RhB dye was determined with a UV−vis spectrophotometer at $\lambda_{max} = 553$ nm.

The photocatalytic mechanism was investigated *via* trapping experiments of the main active species. Various scavengers, namely, benzoquinone (BQ, 10 mM), *tert*-butyl alcohol (TBA, 10 mM), and ammonium oxalate (AO, 10 mM), were added to the aqueous RhB solution containing the catalyst to trap radical anions (O$_2^{\bullet-}$), hydroxyl radicals ($^{\bullet}$OH), and holes (h$^+$), respectively.

3. Results and discussion

3.1. Characterization of materials

The crystalline structures of CN, SNS, and SCNx composites subjected to XRD analysis are shown in Fig. 1a. The XRD pattern of CN shows two distinct prominent peaks around 13.1° and 27.4°, corresponding to the (100) and (002) diffraction crystal planes of graphite-like materials, respectively [2]. Particularly, the broad and weak peak at 2θ = 13.1° corresponds to an in-plane structural packing motif, and the sharp and intense peak at 27.4° originates from the interplanar stacking of π-conjugated aromatic segments [12]. The 2 T-type hexagonal-phase SnS$_2$ (PDF#23-0677) may be indexed to all the major diffraction peaks in the XRD pattern of SNS. However, the characteristic peaks of the g-C$_3$N$_4$ phase are absent in the XRD pattern of SNS, indicating that g-C$_3$N$_4$ in SCN30 is completely decomposed at 650 °C. The main peaks of g-C$_3$N$_4$ and SnS$_2$ are observed in all SnS$_2$/g-C$_3$N$_4$ composites, and no other impurity peaks are detected, demonstrating that their crystal structures are retained after hybridization. The intensity of the (002) peak of g-C$_3$N$_4$ steadily increases as the amount of thiourea added to the precursor mixtures increases, indicating the content of this component in the composites is higher than that of the other components. In general, the XRD results demonstrate that composites with coexisting SnS$_2$ and g-C$_3$N$_4$ are successfully constructed using facile and economic calcination.

The bonding characteristics of the synthesized materials were investigated through FTIR spectroscopy. In Fig. 1b, the FTIR spectrum of CN presents a series of peaks with a strong intensity in the range of 1238–1640 cm^{-1}, which is assigned to the feature stretching vibrations of the C−N and C=N bonds in g-C$_3$N$_4$ heterocycles [13]. Moreover, the typical sharp peaks at 802 and 891 cm^{-1} are involved with bending modes and N−H stretching modes in heptazine units, respectively [19]. The FTIR spectrum of CN also exhibits a wide absorption band at 3000−3300 cm^{-1}, belonging to the N−H stretching vibration modes of the terminal amino groups or O−H bonds of surface-adsorbed water molecules [1]. Notably, the appearance of all the feature peaks of g-C$_3$N$_4$ in SnS$_2$/g-C$_3$N$_4$ composites confirms the absence of the influence of SnS$_2$ introduction on the g-C$_3$N$_4$ structure. The intensity of g-C$_3$N$_4$ peaks in the composite gradually increases from SCN25 to SCN30 and SCN35, implying an increase in the g-C$_3$N$_4$ content in the composite materials. This finding is consistent with the previous XRD discussion. For SNS, a signal with a modest absorption peak is detected at 552 cm^{-1}, corresponding to the characteristic mode of the Sn−S bond. However, this featured signal of SnS$_2$ is invisible in the IR spectra of the composites because of the low relative content of SnS$_2$ [10]. Furthermore, the absorption peaks centered at 2300 cm^{-1} belonging to the stretching vibration of the physically adsorptive CO$_2$ in the atmosphere are recorded in the spectra of the SCNx composites [3,14].
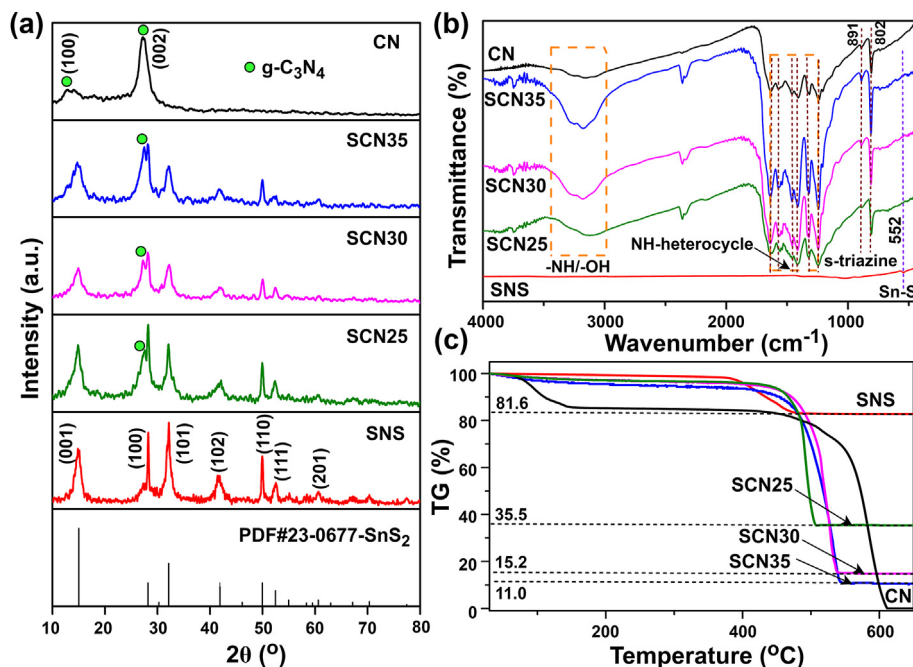
Fig. 1. (a) XRD patterns, (b) FTIR spectra, and (c) TGA of CN, SNS, and SCNx (x = 25, 30 and 35).

The thermostability of CN, SNS, and SCNx samples investigated through TGA analysis is illustrated in Fig. 1c. Two main steps of a total weight loss process are observable in the TGA curves of all the samples. In the first step (from room temperature to 150 °C), physically adsorbed water on a material surface and volatile impurities evaporate. In the second step, SnS_2 oxidizes to SnO_2 (from 350 °C to 540 °C) [15], and g-C_3N_4 thermally decomposes (about 550 °C) [16], thereby causing a considerable weight loss (between 350 °C and 600 °C). The TGA profile of CN shows its intrinsic thermal instability at above 400 °C, and decomposition is completed at 620 °C. In comparison with CN, the second step of the composites occurs at a lower temperature. This result indicates that the thermal stability of g-C_3N_4 in the composite structure likely decreases mainly because of the influence of SnS_2 crystallization on the in-plane structural stacking motif of the g-C_3N_4 phase and the catalytic role of SnS_2 on the partial oxidation of the g-C_3N_4 supporting under air atmosphere. This phenomenon has also been observed in other materials, such as g-C_3N_4/ZnO [17], MoS_2/g-C_3N_4 [18], and In_2O_3/g-C_3N_4 [19]. No remarkable weight loss is observed in the TGA curve of SNS and the composites above 550 °C, confirming that SnS_2 is completely converted to SnO_2. Based on the TGA results, the estimated relative weights of SnS_2 in SNS, SCN25, SCN30, and SCN35 are 98.93 wt%, 43.04 wt%, 18.43 wt%, and 13.34 wt%, respectively (The detailed calculation was shown in Supplementary Information). This finding is consistent with the obtained IR and XRD results, implying that the loading of SnS_2 decreases when the added amount of the g-C_3N_4 (thiourea) source in the as-prepared composites increases.

Fig. 2 illustrates the morphological characteristics and elemental composition of CN and SCN30. In Fig. 2a, a typical SEM image of CN presents bulk morphology of nonuniform layers with a fairly smooth surface stacking them together. This 2D sheet-like structure tends to agglomerate under the given preparation condition. The magnified SEM image of SCN30 (Fig. 2b) shows folded SnS_2 nanoflakes, which grow in stacks with a layer-by-layer structure after they are grafted onto g-C_3N_4. The appearance of SnS_2 nanosheets prevents the aggregation of the g-C_3N_4 substrate,

resulting in an enlarged specific surface on the composite. Accordingly, the pathways of the transport and separation of photoinduced charges between semiconductors may be enhanced. Furthermore, the TEM image of the composite in Fig. 2c reveals that the as-synthesized few-layered SnS_2 nanosheets are less agglomerated and well distributed in the porous g-C_3N_4 matrix. The concentric bright rings of small diffraction spots are visible in the selected area electron diffraction results, corresponding to the (002), (100), (101) (102), and (110) lattice planes and indicating the polynanocrystalline feature of SCN30. The HR-TEM image at a higher magnification of SCN30 (Fig. 2d) presents the lattice fringes of SnS_2 nanosheets with an interlayer spacing of ($d_{(002)}$) plane ranging from 0.59 nm to 0.65 nm. This finding can be attributed to the formation of a large amount of gases emitted during thiourea decomposition, leading to the increased exfoliation and expansion of SnS_2 nanosheets [20]. Elemental mapping was performed to demonstrate SnS_2 dispersion on g-C_3N_4 in the composites. In Fig. 2e_2-4, the elemental mapping images confirm that S, Sn, and N are homogeneously distributed in the as-prepared composite. Overall, these results indicate that the unique nanostructure of the SnS_2/g-C_3N_4 coupled material, which is composed of evenly dispersed SnS_2 nanosheets on the g-C_3N_4 supporting, can significantly enhance the generation and separation of photoexcited charges during photocatalysis.

XPS technique was implemented to determine surface binding properties of CN, SNS, and SCN30 (representative composite). The high-resolution C1s spectrum (Fig. 3a) can be deconvoluted into three characteristic peak components of the carbon atom of g-C_3N_4. The first component with a binding energy of 284.5 eV is attributed to the C=C bonding of the graphitic structure, the second component at 286.2 eV is related to C=N species, and the last component at 288.0 eV corresponds to C sp^2 of N=C−N within the tri-s-triazine ring moieties [20]. Remarkably, these signals also appear in the C1s spectrum of SCN30. The N1s spectrum of CN possesses three contributions (Fig. 3b). In particular, the peak at a binding energy of 398.6 eV corresponds to sp^2-hybridized N (C=N−C) [21], and the peaks at 399.8 and 401.3 eV belong to pyrrolic N
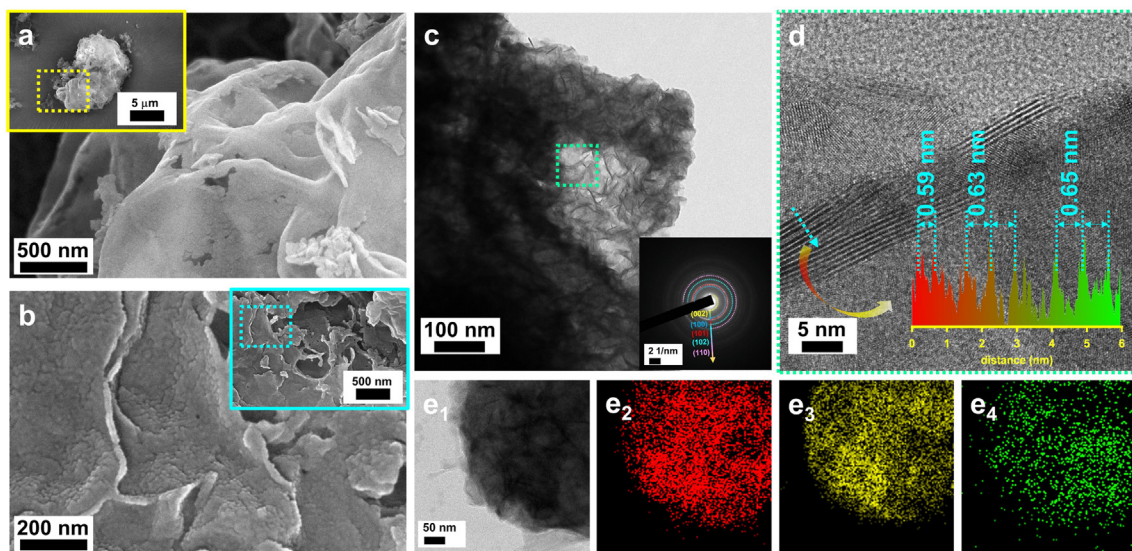
Fig. 2. (a) SEM image of CN. (b) SEM and (c, d) HR-TEM images of SCN30 (inset displaying SAED of c). EDS mapping images of (e$_1$) mapping region (e$_2$) S, (e$_3$) Sn and (e$_4$) N.
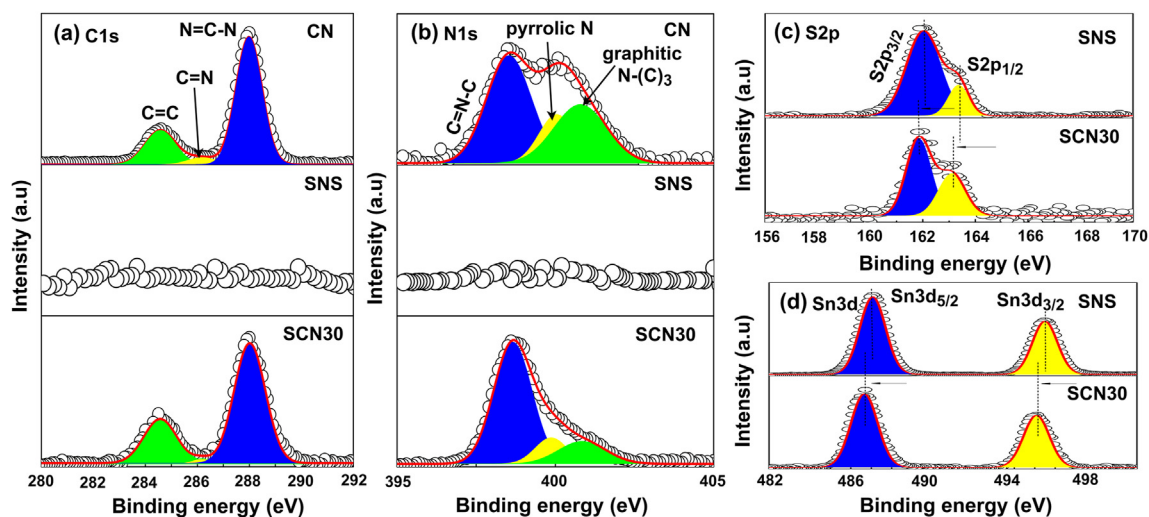

Fig. 3. (a) C1s and (b) N1s XPS spectra of CN, SNS, and SCN30. (c) S2p and (d) Sn3d XPS spectra of SNS and SCN30.

and graphitic tertiary N groups ($N-(C)_3$, $H-N-(C)_2$) or amino functional groups ($C-N-H$), respectively [22]. The S2p XPS signals (Fig. 3c) are fitted into the peaks centered at 161.8 eV (S2p$_{3/2}$) and 163.1 eV (S2p$_{1/2}$), which are associated with S^{2-} chemical states in the SnS$_2$ lattice [15]. Fig. 3d illustrates the high-resolution spectrum of Sn3d with peaks at 486.7 and 495.1 eV, indicating the Sn3d$_{5/2}$ and Sn3d$_{3/2}$ core levels, respectively; thus, these findings confirm the existence of the Sn^{4+} valence state in SNS [23]. Interestingly, the binding energy of Sn3d and S2p of SCN30 negatively shifts compared with that of SNS, suggesting that electrons migrate between g-C$_3$N$_4$ and SnS$_2$ at their heterojunction interface [24]. This may contribute to charge separation in photocatalytic reactions. Thus, the XPS data strongly support the results obtained through XRD and FTIR, which provide clear evidence of the coexistence of two components (SnS$_2$ and g-C$_3$N$_4$) in the composite. Additionally, stability of the composites was studied. Accordingly, the SCN30 sample stored in a vial with closed cover for 5 months was characterized using XRD. The simultaneous presence of the two distinct diffraction peak systems corresponding to the two components of SnS$_2$ and g-C$_3$N$_4$ can be observed in Fig. S1. This result shows no

significant change in the crystal structure compared to the initial SCN30 composite, confirming the stability of SnS$_2$/g-C$_3$N$_4$.

3.2. Photocatalytic activities

In this study, the photocatalytic performance of all the samples was evaluated through RhB photodegradation under visible light irradiation. In Fig. 4a, 37.01% and 45.70% of RhB are decomposed after 6 h of irradiation of SNS and CN, respectively. The RhB degradation percentages of all SnS$_2$/g-C$_3$N$_4$ composites are superior to those of the separated components. Among these photocatalysts, SCN30 exhibits the highest RhB degradation efficiency of 92.22%. For comparison, two controlled experiments were carried out: one without visible light irradiation and the other without photocatalyst addition. The results reveal that RhB can be negligibly degraded in the two cases, suggesting that the degradation efficiency of RhB is attributed to the photocatalytic reaction in the presence of coexisting photocatalyst and light photon. Traditionally, a Langmuir–Hinshelwood model is used to assess the kinetics of photocatalytic progress. A linear relationship between ln (C$_0$/C)
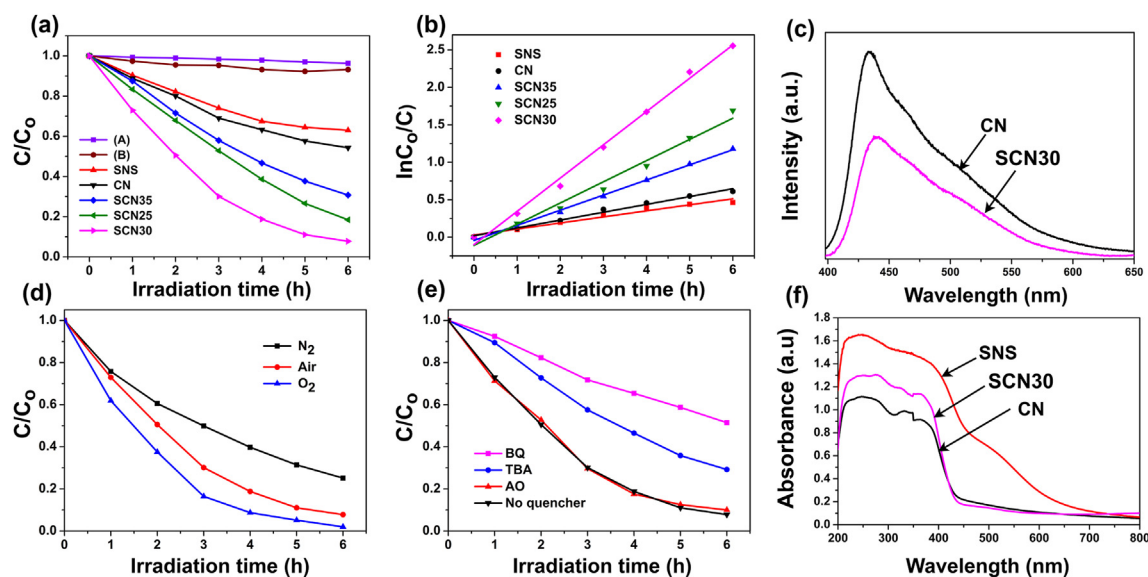
Fig. 4. (a) Photocatalytic degradation of RhB for CN, SNS, SCNx (x = 25, 30 and 35), without (A) photocatalyst and (B) irradiation. (b) The RhB degradation kinetics plots of different catalysts. (c) The PL spectra of CN and SCN30. (d) Photocatalytic degradation of RhB for SCN30 in air, N_2 and O_2 purge. (e) The impact of various scavengers on the RhB degradation activity of SCN30. (f) UV-vis diffuse reflectance spectra of CN, SNS and SCN30.

and the irradiation time t of the samples is shown in Fig. 4b. Accordingly, the obtained data are well fitted with the pseudo-first-order kinetic reaction shown in the following equation: ln $(C_o/C) = k \cdot t$, where C_o and C refer to the initial and measured concentrations of RhB after irradiation time t, respectively, and k is the rate constant. k of all the composites is much greater than that of any single component, confirming the outstanding photocatalytic capability of SnS_2/g-C_3N_4 heterogeneous semiconductors. Among the composites, SCN30 has the highest reaction rate constant (0.44402 h^{-1}), which is about 1.57 and 2.20 times higher than those of SCN25 (0.28279 h^{-1}) and SCN35 (0.20179 h^{-1}), respectively (Table S1). This phenomenon suggests that a reasonable amount of the g-C_3N_4 supporting enhances the transfer and separation channels of photoinduced carriers, thereby improving photocatalytic behavior. However, the overuse of the g-C_3N_4 substrate in the composite can diminish the photocatalytic activity of RhB removal because its properties are similar to those of bare g-C_3N_4 [25]. Another reason is that excessive g-C_3N_4 loading can trigger the shielding effect of g-C_3N_4 on SnS_2, leading to decreased light absorption and limited contact between SnS_2 and oxidative species [7]. The effect of pH on the photocatalytic activity of a representative sample, SCN30 was investigated, indicating that the maximum degradation of RhB was obtained at pH of about 3.8 closing to the pH of RhB solution. A decrease in degradation efficiency was observed when increasing pH (Fig. S2). To enable the degradation of RhB on the catalysts under visible-light irradiation only due to photocatalytic reaction, the adsorption on the photocatalysts was demonstrated (Fig. S3).

The steady-state photoluminescence (PL) spectra of CN and SCN30 were obtained under an excitation wavelength of 355 nm to further demonstrate the extension in the lifetime of charge carriers. In Fig. S4, the PL spectrum of CN can be deconvoluted into four symmetric Gaussian peaks centered at A (433.8 nm, 2.86 eV), B (455.9 nm, 2.72 eV), C (488.5 nm, 2.54 eV), and D (523.6 nm, 2.37 eV). Previous studies showed that the electronic band states of g-C_3N_4 consist of the σ band (sp^3 C–N bond), π band (sp^2 C–N bond), and lone-pair (LP) electrons of bridge N atoms [26]. The four emission peaks (in the order from A to D) of CN reflect different transitions, namely, σ* conduction band (CB)→σ valence band

(VB), σ*→LP, π*→PL, and π*→π, respectively [27,28]. The measured emission energy of the B peak is 2.72 eV, which is similar to the bandgap energy of CN from its UV−vis DRS spectrum. The energy to form the PL emission of g-C_3N_4 can be released by the recombination of photogenerated charges as a result of C vacancies and unpaired lone electrons [7]. In Fig. 4c, CN has a strong emission peak at around 450 nm, suggesting its serious electron−hole recombination rate [23]. However, the intensity of this featured emission peak decreases significantly after the SCN30 composite is constructed. This finding confirms that the presence of SnS_2 in the composite efficiently reduces the recombination of excited electron−hole pairs, thus improving the performance of the photocatalytic system.

The role of dissolved oxygen in the removal efficiency of RhB was evaluated using SCN30 as a representative sample. The solution was purged continuously with nitrogen or oxygen before and after irradiation. Fig. 4d shows that the RhB degradation rate on SCN30 in air reaches around 92.22% and increases significantly to 98.02% with O_2 purging. Only 74.86% of RhB is degraded in the presence of N_2 stream after 6 h of irradiation. In addition, the experimental results fitted with the pseudo-first-order kinetics reveal the highest value of constant rate in the experiment with O_2 (k = 0.65055 h^{-1}), which is around 1.47 and 2.88 times higher than those in air (0.44402 h^{-1}) and N_2 (0.22589 h^{-1}), respectively (Fig. S5a). This result confirms that O_2 contributes to photocatalytic RhB degradation, which can simply capture excited electrons on the CB of semiconductors, thus inhibiting the electron−hole recombination probability. Furthermore, the effects of primary reactive species on the photocatalysis of SCN30 under visible light irradiation were studied. Herein, three chemicals, i.e., BQ, TBA, and AO, were added as quenchers of $O_2^{\bullet-}$, $^\bullet OH$, and h^+, respectively. The results shown in Fig. 4e demonstrate that the photodegradation efficiency of RhB decreases in the presence of scavengers. Remarkably, after 6 h of irradiation, the degradation efficiency decreases considerably to 48.55% with the added BQ, and the photocatalytic efficiency decreases to 70.81% in the presence of TBA. By contrast, the RhB degradation percentage does not significantly change when AO is used. In Fig. S5b, the reaction rate constants show the following trend: AO (0.41022 h^{-1}) > TBA (0.21330 h^{-1}) > BQ (0.11185 h^{-1}). These results determine that $O_2^{\bullet-}$

and $^{\bullet}OH$ are the dominant reactive species, whereas h^+ negligibly influences RhB photodegradation.

The optical properties of the materials were examined through UV−vis DRS spectroscopy (Fig. 4f) to further understand the enhancement in the photocatalytic properties of the obtained heterojunction system. CN displays a strong absorption edge at a wavelength of approximately 450 nm, which corresponds to an intrinsic bandgap energy of about 2.72 eV. The value of the bandgap of CN is consistent with the previously reported results [7,9]. By contrast, SNS has a broad absorption edge of up to 650 nm because of its narrow bandgap (about 1.89 eV). The absorption curves of the composites are similar to those of CN (Fig. S6) because of the coating of the g-C$_3$N$_4$ supporting on SnS$_2$. The bandgap energy of semiconductors can be calculated on the basis of the Kubelka−Munk function equation S1 and is listed in Table S2, indicating that the obtained materials can be activated under visible light condition. The obtained data on the flat band potentials of g-C$_3$N$_4$ and SnS$_2$ are calculated using equations S2 and S3 and presented in Table S3. The CB and VB positions of the two semiconductors are illustrated in Fig. 5.

A photocatalytic mechanism can be proposed on the basis of the aforementioned studies on radical species trapping and bandgap energy. In Fig. 5, two coupled semiconductors present staggered band structures. Their charge transfer behavior is discussed in detail in two ways. The first system is a conventional type-II charge transfer mode (Fig. 5a). In this case, both semiconductors are simultaneously excited to create photoinduced electrons and holes under light irradiation. Then, the CB excited-state electrons of g-C$_3$N$_4$ can transport to the CB of SnS$_2$, whereas the VB photoinduced holes from SnS$_2$ can migrate to the VB of g-C$_3$N$_4$. Accordingly, photogenerated electrons likely accumulate on the CB of SnS$_2$ with a low reduction potential, whereas photogenerated holes tend to accumulate on the VB of g-C$_3$N$_4$ with a low oxidation potential. This transfer mode reduces the redox ability of the composite, leading to a low driving force toward specific photocatalytic reactions. Therefore, the electrons on the CB of the SnS$_2$ semiconductor with a more positive reduction potential than the standard reduction potential of $E°(O_2^{\bullet-}/O_2) = 0.33$ eV (vs. NHE) [10] cannot directly interact with O_2 to produce $O_2^{\bullet-}$ radicals. In comparison with the experimental results on radical suppression, the traditional type-II model is inconsistent because the signal of the main active species ($O_2^{\bullet-}$) is not found. The charge transfer mechanism in a heterostructure system operating in this mode is also problematic from a dynamic perspective because of the significant electrostatic
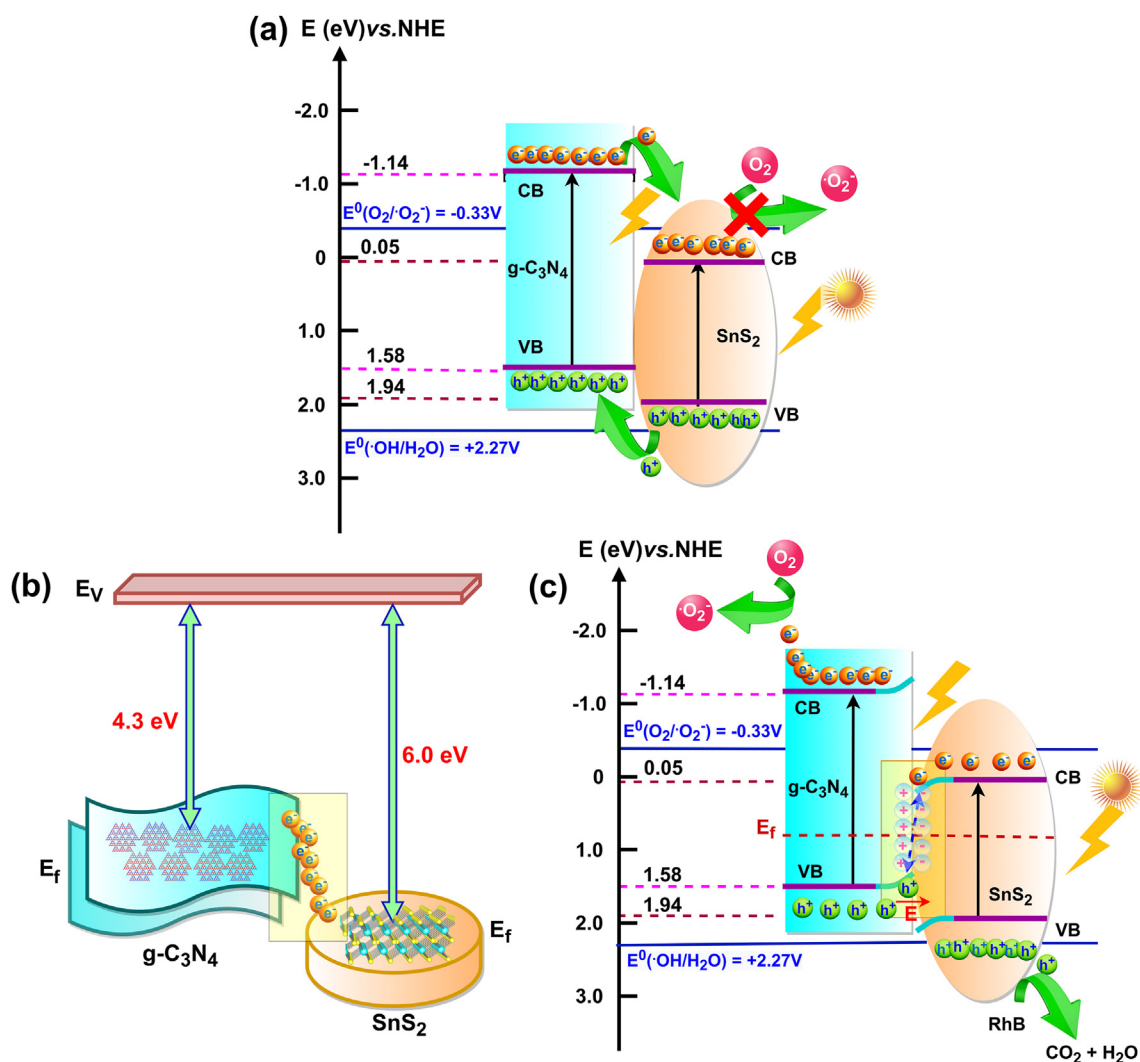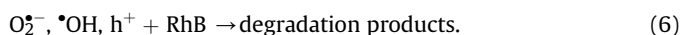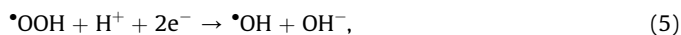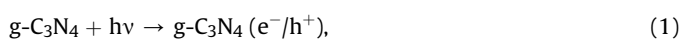

Fig. 5. The schematic diagrams of (a) type-II and (c) S-scheme photocatalytic mechanisms on the SnS$_2$/g-C$_3$N$_4$ composite. (b) Electron transformation due to different Fermi levels between two semiconductors.

repulsion between electrons and holes [29]. In the second system, the S-scheme mechanism is analogous to the type-II system but involves an entirely different charge migration pathway (Fig. 5b,c). According to density functional theory calculations, the Fermi energy (E_f) of SnS_2 with a work function of 6.0 eV is higher than that of g-C_3N_4 with a work function of 4.3 eV [30]. Therefore, after g-C_3N_4 combines with SnS_2, electrons tend to accumulate on the SnS_2 site, leading to a depleted region on g-C_3N_4 at their heterojunction interface to accomplish E_f balance (Fig. 5b). Consequently, the g-C_3N_4 surface is positively charged, whereas the SnS_2 surface is negatively charged at their interface. This charge redistribution results in the formation of an internal electric field (IEF) at the heterostructure interface in the g$-C_3N_4-$to-SnS_2 direction. The IEF can promote interfacial charge transfer, so their separation is greatly enhanced. As a result of charge redistribution, g-C_3N_4 and SnS_2 exhibit upward and downward band bending, respectively. Photoexcited electrons and holes are produced in both semiconductors under visible irradiation. The photoinduced electrons from the CB of SnS_2 can easily transport to the VB of g-C_3N_4 and quickly and strongly recombine with the photoinduced holes because of all the driving forces, including electric field, Coulomb attraction, and force synergistic influence of band bending at the interface. Ultimately, the CB electrons in g-C_3N_4 with a stronger reduction ability and the VB holes in SnS_2 with a greater oxidation ability are preserved. Therefore, the accumulated electrons on the CB of g-C_3N_4 with more negative potential than the standard redox value of $E°(O_2^{\bullet-}/O_2) = 0.33$ eV (*vs.* NHE) can reduce adsorbed O_2 molecules to $O_2^{\bullet-}$. Afterward, $O_2^{\bullet-}$ radicals are protonated to create hydroperoxy radicals ($^{\bullet}OH_2$) and then generate $^{\bullet}OH$ hydroxyl radicals, which are strong oxidative agents in organic dye degradation [9]. Unfortunately, the positive holes in the VB of SnS_2 and g-C_3N_4, which have a greater negative VB potential than the standard redox potential of $E°(^{\bullet}OH/H_2O) = 2.27$ eV (*vs.* NHE) [31], cannot oxidize H_2O to $^{\bullet}OH$. However, the photoinduced holes on the VB of SnS_2 have a minor role in the direct oxidation of RhB. Clearly, the S-scheme separation mechanism of photoexcited charges is consistent with the trapping tests, indicating that $O_2^{\bullet-}$ and $^{\bullet}OH$ radicals remarkably contribute to the photocatalytic degradation of RhB. This process is illustrated in the following reactions:

$$\text{g-}C_3N_4 + h\nu \rightarrow \text{g-}C_3N_4 \ (e^-/h^+), \tag{1}$$

$$SnS_2 + h\nu \rightarrow SnS_2 \ (e^-/h^+), \tag{2}$$

$$e^- \ (\text{g-}C_3N_4) + O_2 \rightarrow O_2^{\bullet-}, \tag{3}$$

$$O_2^{\bullet-} + H^+ \rightarrow {}^{\bullet}OOH, \tag{4}$$

$${}^{\bullet}OOH + H^+ + 2e^- \rightarrow {}^{\bullet}OH + OH^-, \tag{5}$$

$$O_2^{\bullet-}, {}^{\bullet}OH, h^+ + RhB \rightarrow \text{degradation products}. \tag{6}$$

The constructed SnS_2/g-C_3N_4 heterogeneous system with a beneficial synergistic and integrative influence of the two components follows the S-scheme charge transport mechanism instead of the conventional type-II heterojunction structure. Thus, the separation and movement of photogenerated electron$-$hole pairs improve, thereby enhancing the photocatalytic performance of the composite compared with that of the bare photocatalysts (SnS_2 and g-C_3N_4).

4. Conclusion

We proposed a facile one-pot strategy for fabricating SnS_2/g-C_3N_4 semiconductors with various content loadings containing SnS_2 nanosheets distributed on a g-C_3N_4 matrix. The RhB removal efficiency of all the composites was higher than that of bare g-C_3N_4 and SnS_2. Among resultant photocatalysts, the composite, which was prepared with a tin (IV) chloride/thiourea mass ratio of 1:30, exhibited the best performance of 92.22% of RhB photodegradation with a reaction rate constant of 0.44402 h^{-1} in 6 h of irradiation. The effective transfer and separation of photoinduced charges between SnS_2 and g-C_3N_4 in S-scheme heterojunctions is primarily responsible for the increased photocatalytic activity. Therefore, the SnS_2/g-C_3N_4 system is a potential candidate for application in organic pollutant photodegradation.

Declaration of competing interest

The authors declare that they have no known competing financial interests or personal relationships that could have appeared to influence the work reported in this paper.

Appendix A. Supplementary data

Supplementary data to this article can be found online at https://doi.org/10.1016/j.jsamd.2021.11.004.

References

[1] Y. Song, J. Gu, K. Xia, J. Yi, H. Chen, X. She, Z. Chen, C. Ding, H. Li, H. Xu, Construction of 2D SnS_2-g-C_3N_4 Z-scheme composite with superior visible-light photocatalytic performance, Appl. Surf. Sci. 467 (2019) 56–64, https://doi.org/10.1016/j.apsusc.2018.10.118.

[2] J. Wen, J. Xie, X. Chen, X. Li, A review on g-C_3N_4-based photocatalysts, Appl. Surf. Sci. 391 (2017) 72–123, https://doi.org/10.1016/j.apsusc.2016.07.030.

[3] K. Wang, Q. Li, B. Liu, B. Cheng, W. Ho, J. Yu, Sulfur-doped g-C_3N_4 with enhanced photocatalytic CO_2-reduction performance, Appl. Catal. 176 (2015) 44–52, https://doi.org/10.1016/j.apcatb.2015.03.045.

[4] E. Liu, J. Chen, Y. Ma, J. Feng, J. Jia, J. Fan, X. Hu, Fabrication of 2D SnS_2/g-C_3N_4 heterojunction with enhanced H_2 evolution during photocatalytic water splitting, J. Colloid Interface Sci. 524 (2018) 313–324, https://doi.org/10.1016/j.jcis.2018.04.038.

[5] P. Van Viet, H.-P. Nguyen, H.-H. Tran, D.-P. Bui, M.-T. Pham, S.-J. You, C.M. Thi, Constructing g-C_3N_4/SnO_2 S-scheme heterojunctions for efficient photocatalytic NO removal and low NO_2 generation, J. Sci.: Adv. Mater. Dev. (2021), https://doi.org/10.1016/j.jsamd.2021.07.005.

[6] L. Shi, Z. Zhou, Y. Zhang, C. Ling, Q. Li, J. Wang, Photocatalytic conversion of CO to fuels with water by B-doped graphene/g-C_3N_4 heterostructure, Sci. Bull. (2021), https://doi.org/10.1016/j.scib.2021.02.025.

[7] L. Chen, M. Chen, D. Jiang, J. Xie, A facile strategy for SnS_2/g-C_3N_4 heterojunction composite and the mechanism in photocatalytic degradation of MO, J. Mol. Catal. Chem. 425 (2016) 174–182, https://doi.org/10.1016/j.molcata.2016.10.003.

[8] F. Deng, L. Zhao, X. Pei, X. Luo, S. Luo, Facile in situ hydrothermal synthesis of g-C_3N_4/SnS_2 composites with excellent visible-light photocatalytic activity, Mater. Chem. Phys. 189 (2017) 169–175, https://doi.org/10.1016/j.matchemphys.2016.12.028.

[9] Z. Zhang, J. Huang, M. Zhang, Q. Yuan, B. Dong, Ultrathin hexagonal SnS_2 nanosheets coupled with g-C_3N_4 nanosheets as 2D/2D heterojunction photocatalysts toward high photocatalytic activity, Appl. Catal. 163 (2015) 298–305, https://doi.org/10.1016/j.apcatb.2014.08.013.

[10] Y. Liu, P. Chen, Y. Chen, H. Lu, J. Wang, Z. Yang, Z. Lu, M. Li, L. Fang, In situ ion-exchange synthesis of SnS_2/g-C_3N_4 nanosheets heterojunction for enhancing photocatalytic activity, RSC Adv. 6 (2016) 10802–10809, https://doi.org/10.1039/C5RA21506D.

[11] L. Peng, P. Qin, M. Lei, Q. Zeng, H. Song, J. Yang, J. Shao, B. Liao, J. Gu, Modifying Fe_3O_4 nanoparticles with humic acid for removal of Rhodamine B in water,

J. Hazard Mater. 209 (2012) 193–198, https://doi.org/10.1016/j.jhazmat.2012.01.011.

[12] P. Xia, B. Zhu, J. Yu, S. Cao, M. Jaroniec, Ultra-thin nanosheet assemblies of graphitic carbon nitride for enhanced photocatalytic CO_2 reduction, J. Mater. Chem. 5 (2017) 3230–3238, https://doi.org/10.1039/C6TA08310B.

[13] M. Danish, M. Muneer, Facile synthesis of highly efficient Co@ ZnSQDs/g-C_3N_4/MWCNT nanocomposites and their photocatalytic potential for the degradation of RhB dye: efficiency, degradation kinetics, and mechanism pathway, Ceram. Int. 47 (2021) 13043–13056, https://doi.org/10.1016/j.ceramint.2021.01.168.

[14] D. Ayodhya, G. Veerabhadram, Facile fabrication, characterization and efficient photocatalytic activity of surfactant free ZnS, CdS and CuS nanoparticles, J. Sci.: Adv. Mater. Devices 4 (2019) 381–391, https://doi.org/10.1016/j.jsamd.2019.08.006.

[15] Y. Zuo, X. Xu, C. Zhang, J. Li, R. Du, X. Wang, X. Han, J. Arbiol, J. Llorca, J. Liu, SnS_2/g-C_3N_4/graphite nanocomposites as durable lithium-ion battery anode with high pseudocapacitance contribution, Electrochim. Acta 349 (2020) 136369, https://doi.org/10.1016/j.electacta.2020.136369.

[16] G. Angamuthu, E. Jayabal, V. Rengarajan, Electrochemical performance evaluation of carbon nitride synthesized at different temperatures as an anode material for lithium-ion batteries, Ionics 26 (2020) 3863–3873, https://doi.org/10.1007/s11581-020-03566-w.

[17] W. Yu, D. Xu, T. Peng, Enhanced photocatalytic activity of g-C_3N_4 for selective CO_2 reduction to CH_3OH via facile coupling of ZnO: a direct Z-scheme mechanism, J. Mater. Chem. 3 (2015) 19936–19947, https://doi.org/10.1039/C5TA05503B.

[18] H. Tran Huu, X.D. Nguyen Thi, K. Nguyen Van, S.J. Kim, V. Vo, A facile synthesis of MoS_2/g-C_3N_4 composite as an anode material with improved lithium storage capacity, Materials 12 (2019) 1730, https://doi.org/10.3390/ma12111730.

[19] L.-Y. Chen, W.-D. Zhang, In_2O_3/g-C_3N_4 composite photocatalysts with enhanced visible light driven activity, Appl. Surf. Sci. 301 (2014) 428–435, https://doi.org/10.1016/j.apsusc.2014.02.093.

[20] H.T. Huu, H.T. Le, T.H. Nguyen, L.N. Thi, V. Vo, W.B. Im, Facile synthesis of SnS_2@g-C_3N_4 composites as high performance anodes for lithium ion batteries, Appl. Surf. Sci. 549 (2021) 149312, https://doi.org/10.1016/j.apsusc.2021.149312.

[21] G.-D. Shen, Y.-P. Pu, Y.-F. Cui, P.-P. Jing, Easy synthesis of TiO_2/g-C_3N_4 heterostructure photocatalyst with large surface area and excellent photocatalytic activity, Ceram. Int. 43 (2017) S664–S670, https://doi.org/10.1016/j.ceramint.2017.05.243.

[22] V.N. Khabashesku, J.L. Zimmerman, J.L. Margrave, Powder synthesis and characterization of amorphous carbon nitride, Chem. Mater. 12 (2000) 3264–3270, https://doi.org/10.1021/cm000328r.

[23] A. Zhu, L. Qiao, Z. Jia, P. Tan, Y. Liu, Y. Ma, J. Pan, C–S bond induced ultrafine SnS_2 dot/porous gC_3N_4 sheet 0D/2D heterojunction: synthesis and photocatalytic mechanism investigation, Dalton Trans. 46 (2017) 17032–17040, https://doi.org/10.1039/C7DT03894A.

[24] M. Yang, S. Hu, F. Li, Z. Fan, F. Wang, D. Liu, J. Gui, The influence of preparation method on the photocatalytic performance of g-C_3N_4/WO_3 composite photocatalyst, Ceram. Int. 40 (2014) 11963–11969, https://doi.org/10.1016/j.ceramint.2014.04.033.

[25] H.H. Tran, D.H. Truong, T.T. Truong, T. Xuan Dieu Nguyen, Y.S. Jin, S.J. Kim, V. Vo, A facile synthesis of WS_2/g-C_3N_4 composites with improved photocatalytic activity, Bull. Kor. Chem. Soc. 39 (2018) 965–971, https://doi.org/10.1002/bkcs.11536.

[26] W. Wan, J.-Y. Sun, J. Ye, Q.-y. Zhang, Confining the polymerization degree of graphitic carbon nitride in porous zeolite-Y and its luminescence, RSC Adv. 8 (2018) 25057–25064, https://doi.org/10.1039/C8RA04436H.

[27] C. Hu, W.-Z. Hung, M.-S. Wang, P.-J.J. Lu, Phosphorus and sulfur codoped g-C_3N_4 as an efficient metal-free photocatalyst, Carbon 127 (2018) 374–383, https://doi.org/10.1016/j.carbon.2017.11.019.

[28] Y. Zhang, Q. Pan, G. Chai, M. Liang, G. Dong, Q. Zhang, J. Qiu, Synthesis and luminescence mechanism of multicolor-emitting gC_3N_4 nanopowders by low temperature thermal condensation of melamine, Sci. Rep. 3 (2013) 1–8, https://doi.org/10.1038/srep01943.

[29] J. Low, C. Jiang, B. Cheng, S. Wageh, A.A. Al-Ghamdi, J. Yu, A review of direct Z-scheme photocatalysts, Small Methods 1 (2017) 1700080, https://doi.org/10.1002/smtd.201700080.

[30] B. Zhu, H. Tan, J. Fan, B. Cheng, J. Yu, W. Ho, Tuning the strength of built-in electric field in 2D/2D g-C_3N_4/SnS_2 and g-C_3N_4/ZrS_2 S-scheme heterojunctions by nonmetal doping, J. Materiomics (2021) https://doi.org/10.1016/j.jmat.2021.02.015.

[31] Y.-p. Li, F.-t. Li, X.-j. Wang, J. Zhao, J.-n. Wei, Y.-j. Hao, Y. Liu, Z-scheme electronic transfer of quantum-sized α-Fe_2O_3 modified g-C_3N_4 hybrids for enhanced photocatalytic hydrogen production, Int. J. Hydrogen Energy 42 (2017) 28327–28336, https://doi.org/10.1016/j.ijhydene.2017.09.137.